Adaptive Color Structured Light for Calibration and Shape Reconstruction

Xin Dong[*] Southwest University
Haibin Ling[†] Stony Brook University
Bingyao Huang[‡] Southwest University

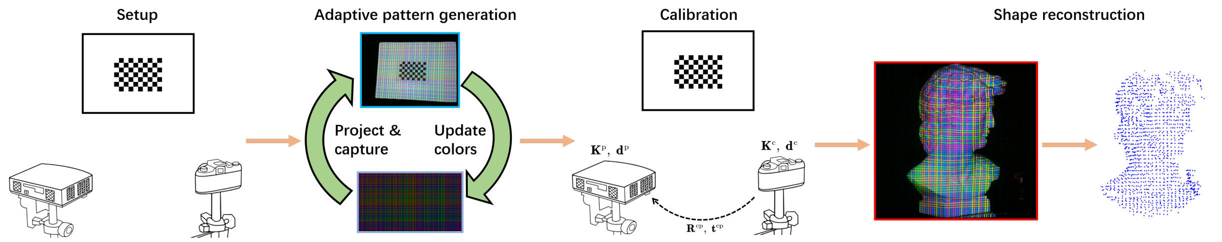

Figure 1: The proposed adaptive color structured light.

ABSTRACT

Color structured light (SL) plays an important role in spatial augmented reality and shape reconstruction. Compared to traditional non-color multi-shot SL, it has the advantage of fewer projections, and can even achieve single-shot. However, distortions caused by ambient light and imaging devices limit color SL's applicability and accuracy. A common solution is to apply color adaptation techniques to cancel the disturbances. Previous studies focus on either robust fixed color patterns or adaptation approaches that may require preliminary geometric calibrations. In this paper, we propose an approach that can efficiently adapt color SL to arbitrary ambient light and imaging devices' color responses, without device response function calibration or geometric calibration. First, we design a novel algorithm to quickly find the most distinct colors that are easily separable under a new environment and device setup. Then, we design a maximum a posteriori (MAP)-based color detection algorithm that can utilize ambient light and device priors to robustly detect the SL colors. In experiments, our adaptive color SL outperforms previous methods in both calibration and shape reconstruction tasks across a variety of setups.

Index Terms: Computing methodologies—Computer vision—Image and video acquisition—Camera calibration; Computing methodologies—Computer vision—Image and video acquisition—Reconstruction;

1 INTRODUCTION

Structured light is an important technique for projector-camera systems, and it is widely used in spatial augmented reality (SAR)/projection mapping [11–13, 16, 18, 25, 27, 30, 31, 34, 35, 38, 40]. Most SAR applications require a preliminary step of SL-based [14, 42] calibration and scene shape recovery. Color SL uses colors to encode projector pixels' spatial information to reduce the number of projections. Thus, in some applications such as dynamic projection mapping [31] and dynamic shape reconstruction [26, 49, 53], color SL is preferred to Gray-coded SL for better performance.

A typical color SL system is shown in Fig. 1, where the projector first projects carefully designed patterns to the target scene. Then, the camera captures the scene along with the superimposed patterns. Finally, the camera-captured images and the projected patterns are matched to obtain the projector-camera pixel correspondences for calibration or shape reconstruction. In practice, the projected SL patterns undergo geometric and photometric distortions due to the setup, i.e., scene geometry, ambient light and color responses of the imaging devices [19, 47, 49], e.g., the camera-captured colors may be significantly deviated from the projected ones if the ambient light, the camera and projector color responses are uncalibrated. These distortions may affect the accuracy and robustness of the pattern matching process. Thus, abundant previous work focuses on designing robust color SL patterns for these scenarios. Despite these efforts, most color SL methods use fixed patterns for all setups without considering the ambient light and device priors, and may still obtain suboptimal results in non-ideal conditions. Moreover, some methods require a preliminary geometric calibration step, which limits the practicability of color SL.

In this paper we propose a practical adaptive color SL to address these issues. Our goal is to find the optimal color combination of the SL pattern according to different setups rather than using a fixed pattern, such that the pattern segmentation and color detection are more robust under different ambient light conditions and projector-camera system's color responses. We first design two quality measures for pattern segmentation and color detection, respectively. For pattern segmentation, we use the ratio between the current and the ideal number of segmented pixels as the segmentation success rate. For color detection, we assume that larger color distinction leads to better detection. Therefore, we proposed a color distinction measure by comparing colors' hue distributions. Our method is shown in Fig. 1, we start by projecting and capturing the color SL pattern, and we update the SL color combinations by optimizing the two measures iteratively. To improve efficiency, we exclude the project-and-capture operation from the optimization loop, and use genetic algorithm (GA) to find the optimal color combination from a set of sampling images. Finally, the optimal color SL pattern is used for projector-camera calibration and shape reconstruction.

Another important issue addressed by our method is a robust color detection algorithm based on ambient light and device priors. Due to the optimal color combination searching step above, we have some prior knowledge about the ambient light and projector-camera system's color responses, therefore we propose a maximum a posteriori estimation (MAP)-based algorithm for color detection. In experiments, our approach shows significant advantages in robustness and success rate compared with simple color thresholding and lookup table-based color detection methods, e.g., [21]. Moreover, unlike most previous work [31, 53], our method does not require a prelimi-

[*]e-mail: dongxin12345@email.swu.edu.cn
[†]e-mail: hling@cs.stonybrook.edu
[‡]e-mail: bhuang@swu.edu.cn. Corresponding author

nary device response function calibration or geometric calibration. In summary, our contributions are as follows:

- We propose an adaptive color SL that can adapt to different ambient light conditions and projector-camera color responses without device response calibration or geometric calibration.
- An MAP-based color detection algorithm is designed to utilize ambient light and device priors to improve SL color detection.
- In experiments, our method outperforms the previous method by higher calibration and reconstruction qualities, especially in non-ideal setups.

The code and dataset are publicly available at `https://github.com/Dongxin000/Adaptive-color-SL`.

2 Related work

SL plays an essential role in SAR and projector-camera systems applications, such as geometric calibration [12,18], response function calibration [6,15], projection mapping [27,31] and shape reconstruction [26,49,53]. Existing SL approaches can be briefly classified into time multiplexing, spatial multiplexing and mixed ones, please refer to [14,42] for more detailed reviews.

Time multiplexing methods project a sequence of patterns to encode each single pixel, and usually use Gray/binary code [39,46] or phase-shifted sinusoidal code [50,54]. Due to multi-shot of SL patterns, those approaches are computationally expensive and usually used in static scenes, despite offering pixel-wise or even sub-pixel dense correspondences.

On the other hand, spatial multiplexing SL uses spatial information to encode pixel locations. Exemplar patterns are checkerboard [1], fringe projection profilometry [22], M-array [2,48] and De Bruijn sequence [20,26,41]. With color encoding techniques, they can further reduce the number of shots [3,6,31,33,43,49], and thus are more suitable for dynamic applications. However, colors are sensitive to ambient light and projector-camera systems' color responses [5,9,19,32,47,49,51,53]. Abundant previous work has been proposed to address this issue, and can be roughly divided into two categories: one type focuses on fixed SL patterns and aims to study more accurate and robust image detection algorithms or to design robust SL patterns; the other is to **adaptively adjust** SL patterns according to the environment and devices' color responses.

Fixed color patterns. For fixed color SL patterns, clustering or thresholding are usually used for color detection [21,24,54]. But due to the disturbances from the ambient light and the imaging devices, these methods may result in suboptimal solutions. Some studies focus on more accurate and robust color detection approaches, e.g., Zhang *et al*. [51] present a decision-directed method to get the initial centroids, which overcomes the converging to local optima issue of K-means. A new strategy by Fechteler *et al*. [10] is proposed to make color detection independent of brightness, thereby reducing interference from object surfaces and ambient light. Fechteler and Eisert [9] improve the previous approach by a robust and adaptive color detection algorithm that can achieve single-shot face reconstruction. Lee *et al*. [32] use Log-gradient filters to reduce the color distortions from the object material. Zhang *et al*. [49] apply multi-pass dynamic programming to decode color stripe SL.

Hu *et al*. [17] design stripes and multi-slit patterns to maximize robustness while minimizing the number of colors and window size. This technique makes the projector-camera system more robust against ambient light and color crosstalk. Chen *et al*. [7] propose three pure color patterns to address the crosstalk between DLP projectors and CCD cameras. Je *et al*. [23] study a single-shot pattern that maximizes the color contrast between stripes, which can reduce the ambiguity caused by system resolutions and object colors. With two shots, their method can further reduce blurriness caused by colored object surfaces, ambient light, projector noise and nonlinear responses. Đonlić *et al*. [54] use multi-shot color self-correcting De Bruijn sequences for robust color detection.

Adaptive color patterns. Adaptive color patterns aim to modify the SL color according to the environment and imaging devices. Koninckx and Gool [28] analyze the setup and the colors of the scene to find easily disturbed colors, and then solve the color that is least susceptible to the colors of the scene to form a pattern. Caspi *et al*. [6] estimate the albedo of the object surface, scene colors and color crosstalk between the projector and the camera. Then, they design a Gray-code based adaptive color SL pattern to reduce the number of shots, but a preliminary response function calibration step is required. Zhou *et al*. [53] present a color calibration method to deal with disturbances from surface albedo and ambient light, thereby improving the accuracy of color SL recognition. By calibrating the response functions of the camera and the projector, Koninckx *et al*. [29] propose an extended projector-camera model to address crosstalk and possible overexposure/underexposure. Kurth *et al*. [31] study a color SL that can adapt to dynamic ambient light and object surface colors. However, most methods above need a preliminary step of response function calibration or geometric calibration.

3 Methods

The overview of our adaptive color SL is shown in Fig. 2, and we will explain the three key ingredients: adaptive pattern generation, MAP-based color detection and calibration and shape reconstruction.

3.1 Adaptive pattern generation

We employ a single color grid pattern (see Fig. 2) for both projector-camera calibration and shape reconstruction. Similar to [21], the color grid pattern uses De Bruijn [8,44] sequence encoding. A De Bruijn sequence is a special type of combinatorial sequence that generates an L-order cyclic sequence of length N^L from an alphabet of N color labels, ensuring that each subsequence of length L appears exactly once. De Bruijn is applied to encode both horizontal and vertical stripes of the color grid pattern. Let $C_1, C_2, ..., C_N$ be the N-color combination encoding the stripes with corresponding color labels $1, 2, ..., N$. By encoding in horizontal and vertical stripes, a color grid of $m_{\text{hori}} \times m_{\text{vert}}$ can be constructed, where $m_{\text{hori}} = N_{\text{hori}}^L + 2$, $m_{\text{vert}} = N_{\text{vert}}^L + 2$ and N_{hori}, N_{vert} are the numbers of color labels for horizontal stripes and vertical stripes, respectively. In our case $L = 3$ for both horizontal and vertical stripes.

To make the color SL more robust against ambient light and imaging devices' color responses, we aim to find the optimal color combination. We assume that a color combination is optimal when each of the different colors can be clearly distinguished, and accurately detected. An intuitive solution is to use parametric optimizations, e.g., gradient descent and Levenberg-Marquardt, but these methods require gradient of the real project-and-capture operation. Clearly, it is nearly impossible to find the analytical gradient, while computing the numerical gradient requires thousands of real project-and-capture operations. As for gradient-free solution, a typical method is to randomly sample N colors from the RGB space to form an SL pattern, and then project and capture the SL pattern, and choose the best color combination that meet our criteria. However, it also needs thousands of real project-and-capture operations, since the RGB space is too large. To make things worse, the real project-and-capture operation is time-consuming, making these solutions more impractical.

To address this issue, we choose N colors to generate the initial color grid pattern. The N colors are separated by the largest equidistant distance on the hue wheel, and are shifted by the same amount together during color update. As shown in Fig. 2, when $N = 4$, the hue values of the four colors are always separated by $360°/N$ on the hue wheel during the optimization loop, and for each iteration, the N colors are shifted by $360°/(N \times K_{\max})$, where $K_{\max} = 5$. Afterwards, we project the color grid pattern to the calibration board and capture it using the camera, i.e., I_{SL}, with which we calculate the

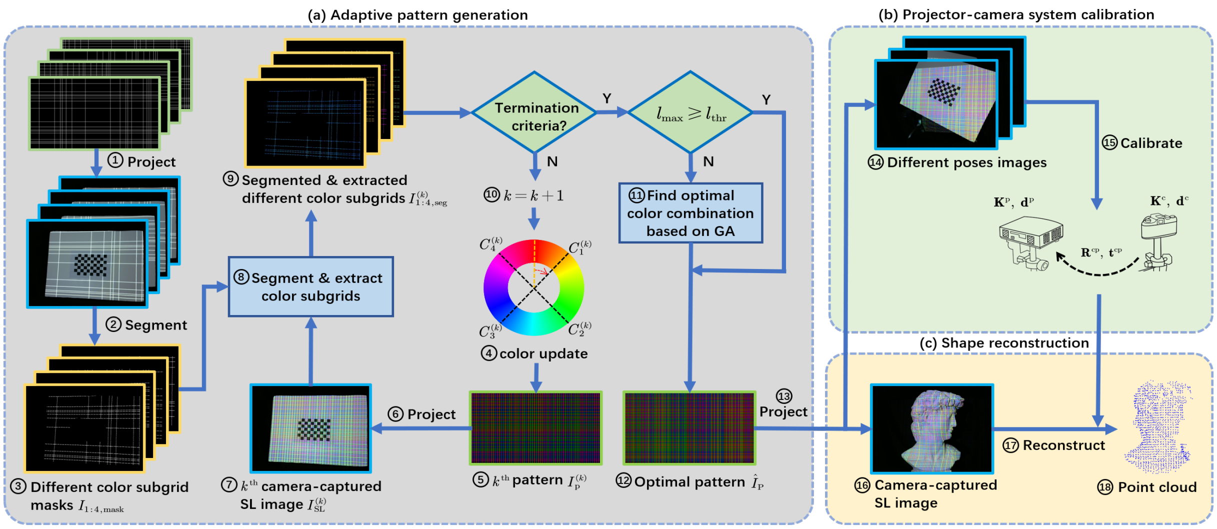

Figure 2: Overview of our adaptive color SL system. Our method can be roughly divided into three parts: (a) adaptive pattern generation, (b) projector-camera system calibration and (c) shape reconstruction. We first project N (e.g., $N = 4$) white subgrid patterns onto the calibration board, and segment them to obtain the corresponding color subgrid masks $I_{1:4,\mathrm{mask}}$ for later use. Then, we update the color combination $C_{1:4}^{(k)}$ of our color grid pattern iteratively. In each iteration, we first project the color grid pattern $I_{\mathrm{p}}^{(k)}$, and capture it as an image $I_{\mathrm{SL}}^{(k)}$. Afterwards, we segment $I_{\mathrm{SL}}^{(k)}$ and extract different color subgrids from it using color subgrid masks $I_{1:4,\mathrm{mask}}$. We analyze the segmented and extracted color subgrids $I_{1:4,\mathrm{seg}}^{(k)}$ and measure whether we reach the maximum number of iterations or the color distinction score is above the desired threshold l_{thr} (i.e., termination criteria). After the iterative adjustment, if the final color distinction score $l_{\max}$ is still lower than the desired optimal score threshold l_{thr}, we use GA to efficiently search for the optimal color combination among all observed colors. Finally, our optimal color grid pattern $\hat{I}_{\mathrm{p}}$ is generated using the optimal color combination, and used for (b) projector-camera system calibration and (c) shape reconstruction.

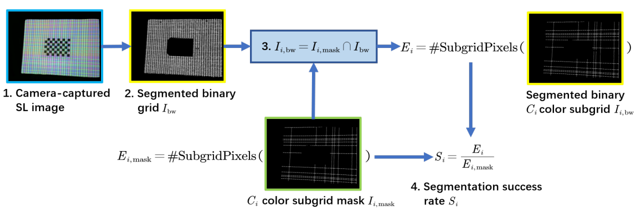

Figure 3: Segmentation success rate calculation. **(1)** Capture the scene with a color grid pattern as an SL image. **(2)** Segment the color grid to obtain the binary grid I_{bw} from SL image. **(3)** Use the C_i color subgrid mask $I_{i,\mathrm{mask}}$ to extract the binary C_i color subgrid $I_{i,\mathrm{bw}}$ from I_{bw}. **(4)** Calculate S_i for C_i color using the number of subgrid pixels of the C_i color subgrid mask $I_{i,\mathrm{mask}}$ and the C_i color subgrid $I_{i,\mathrm{bw}}$.

segmentation success rate and color distinction score. The above steps are repeated until the termination criteria are met, i.e., reaching the maximum number of iterations or the desired color distinction score threshold, as shown in Alg. 1 stage 1. If the desired color distinction score threshold is not met at the maximum number of iterations, we use GA to find an N-color combination that maximizes the color distinction score, as shown in Alg. 1 stage 2. Finally, the optimal SL pattern is generated by the N-color combination with the best color distinction score. At most 5 patterns are projected during the whole process, which is much more efficient than solutions that involve thousands of real project-and-capture operations. It is worth noting that we only need to generate adaptive pattern once, unless the imaging device settings or the ambient light conditions change.

We then explain the two quality measures (criteria) for the optimal color combination: segmentation success rate S_i and color distinction score l. Let the initial N-color combination be: $C_1, C_2, \ldots, C_N$, where $N \geq 3$ is a user-specified number of colors and $C_i = (R_i, G_i, B_i)$ is the RGB value of the i-th candidate color of the projector input pattern stripes. Our segmentation success rate is defined as follows. By segmenting the camera-captured color grid's subgrids, we get the segmentation success rate of each color subgrid $S_i = \frac{E_i}{E_{i,\mathrm{mask}}}$, where $E_{i,\mathrm{mask}}$ and E_i are the number of pixels, which have color C_i in image $I_{i,\mathrm{mask}}$ and $I_{i,\mathrm{bw}}$, respectively, as shown in Fig. 3. The operation is defined as **CalSegmentationSuccessRate** in Alg. 1.

Ideally, the camera-captured color grid in SL image I_{SL} should have the same RGB values as the projected one I_{p}, however, due to the ambient light and color responses of imaging devices, the camera-captured color grid colors are clearly not the same as the projected ones (e.g., compare subfigures 1 and 6 in Fig. 4), and even the pixel values on the same stripe may vary. Thus, a simple color lookup table and hard thresholding-based detection method are suboptimal. To address this issue, we find the optimal N-color combination according to the setup, followed by a MAP-based color detection algorithm for robust SL pattern decoding. We start by converting the camera-captured color grid from RGB to HSV, and for each color C_i we bin its pixel hues and construct a 256-bin histogram $\mathbf{Q}_i \in \mathbb{R}^{1\times 256}$ as shown in Fig. 5. The operation is defined as **FindColorDistribution** in Alg. 1. Afterwards, we normalize $\mathbf{Q}_i$ to a feature vector by $\mathbf{V}_i = \frac{\mathbf{Q}_i}{\|\mathbf{Q}_i\|_2}$, and the similarity between two color distributions is defined as $\mathcal{D}(\mathbf{Q}_i, \mathbf{Q}_j) = \mathbf{V}_i \cdot \mathbf{V}_j$, where $\cdot$ is the dot product of two vectors. Then, color distinction score l is:

$$l = \sum_{i \neq j} (1 - \mathcal{D}(\mathbf{Q}_i, \mathbf{Q}_j)) \tag{1}$$

Our goal is to make the N colors in the camera-captured color grid images distinct by maximizing l. Moreover, to better segment the color grid, we add a constraint that the grid segmentation success rate S_i must be greater than the grid segmentation success rate threshold T_{seg}. Then, the optimal N-color combination is found by iteratively optimizing the following objective function:

$$\hat{C}_1, \hat{C}_2, \ldots, \hat{C}_N = \underset{C_1, C_2, \ldots C_N}{\arg\max}\, l \quad \text{s.t. } S_i \geq T_{\mathrm{seg}} \tag{2}$$

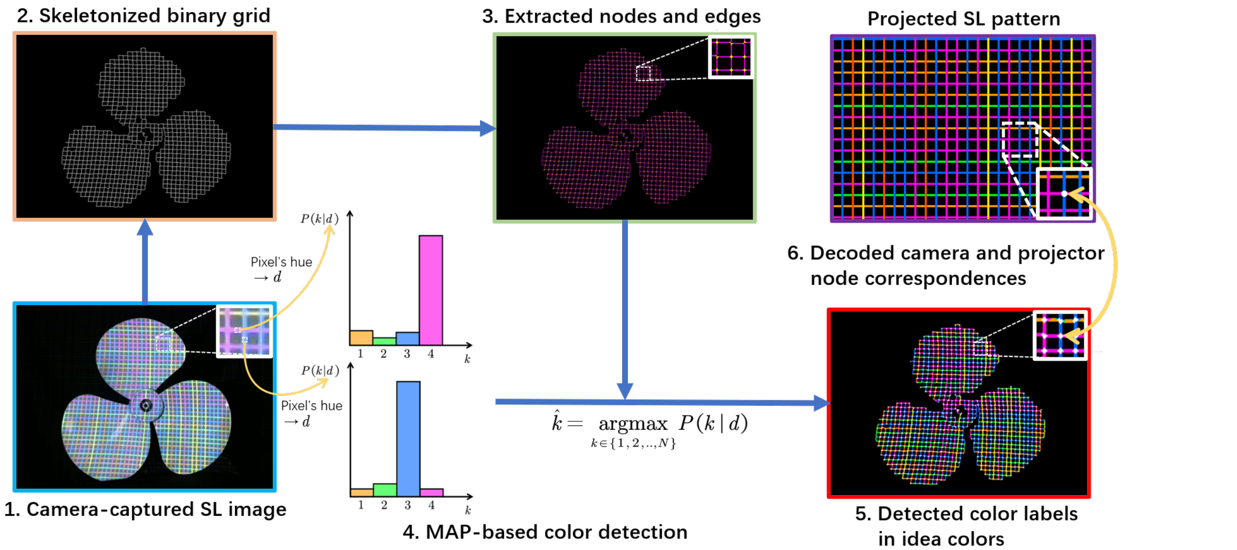

Figure 4: Finding SL correspondences using MAP-based color detection. **(1)** Capture the scene with an adaptive color SL pattern. **(2)** Skeleton the grid of SL image. **(3)** Extract grid nodes (stripe intersections) and edges (stripe segment connecting two nodes). **(4)** Detect the edges' color of the grid using MAP-based color detection – identify the pixel color label by maximizing posterior probability $P(k|d)$. **(5)** Display the color detection result using idea colors. **(6)** Decode and identify the node correspondences between the camera image and projector image based on De Bruijn [8, 44].

The detailed algorithm is shown in Alg. 1. It should be noted that in stage 2, if the optimal color distinction score of stage 1 does not reach the desired optimal score threshold, we use GA to search for an optimal N-color combination by optimizing Eq. 2 among all the observed colors in stage 1. Finally, the optimal color grid pattern $\hat{I}_\text{p}$ is generated using the optimal N-color combination and used for system calibration and shape reconstruction.

3.2 MAP-based color detection

Color detection is the key to finding the correct projector-camera pixel correspondences. Another advantage of our adaptive color SL is a robust color detection algorithm that can leverage the ambient light and device priors embedded in the optimal N-color combination $\hat{C}_1, \hat{C}_2, ..., \hat{C}_N$ and hue distributions $\hat{\mathbf{Q}}_1, \hat{\mathbf{Q}}_2, ..., \hat{\mathbf{Q}}_N$.

Denote d as the hue of a camera-captured pixel, $k \in \{1, 2, ..., N\}$ as the true color label of a camera-captured pixel. Then, $P(k)$ is the probability of a camera-captured pixel's true color label being k. $P(d)$ is the probability of a camera-captured pixel's hue being d. $P(d|k)$ is the conditional probability of a camera-captured pixel's hue is d given its true color label is k. The detected color label $\hat{k}$ can be obtained using maximum likelihood:

$$\hat{k} = \underset{k\in\{1,2,...,N\}}{\arg\max}\ P(d|k). \tag{3}$$

However, our color grid pattern has an imbalanced number of different color stripes. Considering this prior, we instead use *maximum a posteriori estimation* (MAP) for a more accurate detection:

$$P(k|d) = \frac{P(d|k)P(k)}{P(d)}, \quad \hat{k} = \underset{k\in\{1,2,..,N\}}{\arg\max}\ P(k|d) \tag{4}$$

where $P(k)$, $P(d)$ and $P(d|k)$ are given by:

$$P(k=i) = \frac{\sum_j \hat{\mathbf{Q}}_i(j)}{\sum_i \sum_j \hat{\mathbf{Q}}_i(j)}, \ P\left(d \in [d_{j-1}, d_j]\right) = \frac{\sum_i \hat{\mathbf{Q}}_i(j)}{\sum_i \sum_j \hat{\mathbf{Q}}_i(j)}, \tag{5}$$

$$P\left(d \in [d_{j-1}, d_j] | k = i\right) = \frac{\hat{\mathbf{Q}}_i(j)}{\sum_j \hat{\mathbf{Q}}_i(j)}, \tag{6}$$

where $j \in \{1, 2, ..., 256\}$ is the index of the histogram bins, and $[d_{j-1}, d_j]$ is the lower and upper bounds of each bin, as shown in Fig. 5. The MAP-based color detection algorithm is shown in Fig. 4 step 4.

Algorithm 1: Adaptive pattern generation

Input:
N: number of colors
K_max: maximum number of iterations
l_thr: desired optimal score threshold
$C_{1:N}$: initial N colors
$I_{1:N,\text{mask}}$: color subgrid masks
Output: $\hat{C}_{1:N}$; $\hat{\mathbf{Q}}_{1:N}$

```
Initialize: k = 1; l_max = 0; T_seg = 0.8; C^(1)_{1:N} ← C_{1:N};
// Stage 1. Project & capture
while k ≤ K_max and l_max < l_thr do
    I^(k)_p = GeneratePattern(C^(k)_{1:N}) ;
    I^(k)_SL = ProjectAndCapture(I^(k)_p) ;
    S^(k)_{1:N} = CalSegmentationSuccessRate(I^(k)_SL, I_{1:N,mask});
    Q^(k)_{1:N} = FindColorDistribution(I^(k)_SL, I_{1:N,mask});
    l = Σ_{i≠j} (1 − D(Q^(k)_i, Q^(k)_j));
    if ∀S^(k)_i ≥ T_seg and l > l_max then
        l_max ← l ;
        Ĉ_{1:N} ← C^(k)_{1:N};
        Q̂_{1:N} ← Q^(k)_{1:N};
    end
    k ← k + 1;
    C^(k)_{1:N} = UpdateColors(C^(k−1)_{1:N});
end
// Stage 2. Find optimal N-color combination based on GA
if l_max < l_thr then
    Ĉ_{1:N}, Q̂_{1:N} = GA(C^(1:K_max)_{1:N}, Q^(1:K_max)_{1:N}, N);
end
```

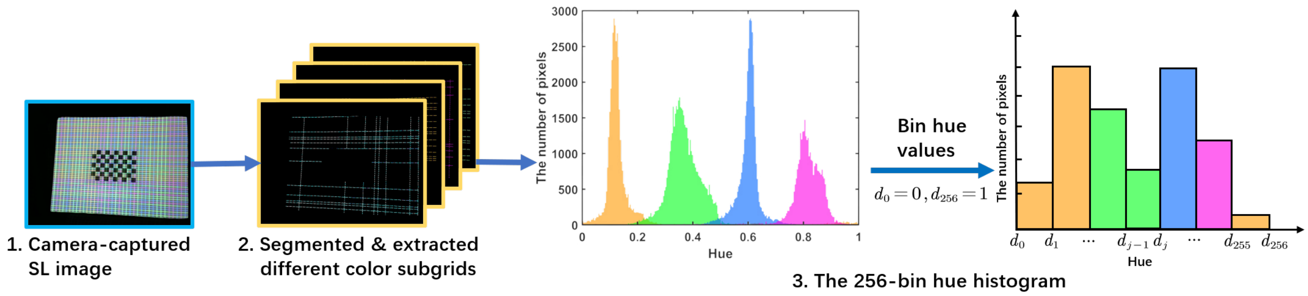

Figure 5: The 256-bin hue histogram construction of different colors. **(1)** Capture the scene with a color grid pattern as a SL image. **(2)** Segment and extract different color subgrids from SL image using color subgrid masks $I_{1:4,\text{mask}}$. **(3)** Bin pixel hue values and construct a 256-bin hue histogram as the distribution of the number of pixels of different hues based on the color subgrids for different colors.

Imaging setting	Setting1	Setting2	Setting3	Setting4	Setting5	Setting6	Setting7
Sample image	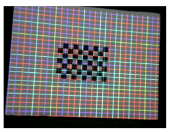	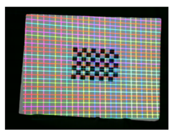	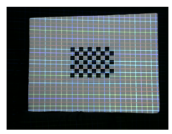	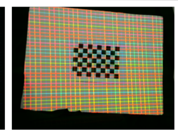	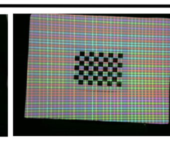	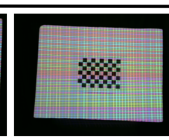	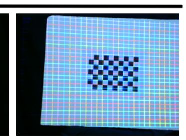
Resolution	Camera: 640*480 Projector: 800*600	Camera: 640*480 Projector: 800*600	Camera: 640*480 Projector: 1024*768	Camera: 640*480 Projector: 1024*768	Camera: 960*720 Projector: 1400*1050	Camera: 1280*960 Projector: 1920*1080	Camera: 640*480 Projector: 800*600
White balance	Camera: 4000K Projector: 6500K	Camera: 4000K Projector: 6500K	Camera: 4000K Projector: 10000K	Camera: 10000K Projector: 5000K	Camera: 4300K Projector: 6500K	Camera: 4300K Projector: 6500K	Camera: 0K Projector: 10000K
Camera saturation	35	73	20	74	47	47	73
Projector color adjustment	RGB=(0, 0, 0)	RGB=(0, 0, 0)	RGB=(-16, -16, 16)	RGB=(16, -16, -16)	RGB=(0, 0, 0)	RGB=(0, 0, 0)	RGB=(-16, -16, 16)

Figure 6: Different imaging settings used for comparison. See supplementary for more poses.

3.3 Calibration and shape reconstruction

Calibration aims to obtain the intrinsic and extrinsic parameters of the projector-camera pair, such as the intrinsic matrices, lens distortion coefficients and relative rotation and translation, and it is essential for projection mapping and shape reconstruction applications. Our calibration method follows the one in [20] and assumes that the world origin is in the optical center of the camera, and adopts a right-hand coordinate system for modeling the camera, projector, and calibration board model spaces. To make the paper self-contained, we briefly introduce the processes below.

The superscripts $^{\mathrm{c}}, ^{\mathrm{p}}$ and $^{\mathrm{m}}$ represent camera, projector, and calibration board model space respectively throughout the paper. The transformation from the camera (or calibration board) coordinate system to the projector coordinate system is represented by the superscript cp (or mp). $\mathbf{K}^{\mathrm{c}}$ and $\mathbf{K}^{\mathrm{p}}$ respectively define the intrinsic matrices of the camera and the projector. The camera and projector's distortion coefficients are $\mathbf{d}^{\mathrm{c}} = [k_1, k_2, p_1, p_2], \mathbf{d}^{\mathrm{p}} = [k_1', k_2', p_1', p_2']$, where k_1, k_1' and k_2, k_2' are radial distortion factors; p_1, p_1' and p_2, p_2' are tangential distortion factors. The extrinsic parameters are relative rotation $\mathbf{r}^{\mathrm{cp}} = [r_x, r_y, r_z]^T$ and translation $\mathbf{t}^{\mathrm{cp}} = [t_x, t_y, t_z]^T$ of the camera with respect to the projector.

After obtaining the optimal color grid pattern, first, for each calibration board pose, we project and capture the pattern. Then, we decode the pattern and find 2D point correspondences between the projector and the camera images. Afterwards, we calibrate the camera and the projector using Zhang's method [52] to get a good initial estimation. Finally, the intrinsic and extrinsic parameters are jointly optimized using bundle adjustment to minimize the impact of the imperfect planarity of the calibration board's surface.

The bundle adjustment (BA) loss function in Eq. 11 is defined as:

$$\text{loss}_{\text{BA}} = \sum_{j=1}^{N_{\text{pose}}} \sum_{i=1}^{M_j} \left(\delta_j^{\mathrm{c}}(\mathbf{x}_i) + \delta_j^{\mathrm{p}}(\mathbf{x}_i) + \lambda\, \delta_j^{\mathrm{m}}(\mathbf{x}_i) \right), \tag{7}$$

where $\delta_j^{\mathrm{c}}(\mathbf{x}_i)$ (Eq. 8) and $\delta_j^{\mathrm{p}}(\mathbf{x}_i)$ (Eq. 9) are reprojection errors of the color grid intersection $\mathbf{x}_i$ in the camera and projector image space, respectively; $\delta_j^{\mathrm{m}}(\mathbf{x}_i)$ (Eq. 10) is a necessary scale constraint that bounds the scale of SL node coordinates $\mathcal{X}^{\mathrm{m}}_{1:N_{\text{pose}}}$ during bundle adjustment since $\mathcal{X}^{\mathrm{m}}_{1:N_{\text{pose}}}$ is coupled with translation vectors $\mathbf{t}^{\mathrm{cp}}_{1:N_{\text{pose}}}$. The weight λ is set empirically as $\lambda = \exp\left(-\delta_j^{\mathrm{m}}(\mathbf{x}_i)\right)$.

$$\delta_j^{\mathrm{c}}(\mathbf{x}_i) = \left\| \mathcal{X}_j^{\mathrm{c}}(\mathbf{x}_i) - \pi\left(\theta^{\mathrm{c}}; \mathcal{X}_j^{\mathrm{m}}(\mathbf{x}_i)\right) \right\|^2, \tag{8}$$

$$\delta_j^{\mathrm{p}}(\mathbf{x}_i) = \left\| \mathcal{X}_j^{\mathrm{p}}(\mathbf{x}_i) - \pi\left(\theta^{\mathrm{p}}, \mathbf{r}^{\mathrm{mc}}_{1:N_{\text{pose}}}, \mathbf{t}^{\mathrm{mc}}_{1:N_{\text{pose}}}; \mathcal{X}_j^{\mathrm{m}}(\mathbf{x}_i)\right) \right\|^2, \tag{9}$$

$$\delta_j^{\mathrm{m}}(\mathbf{x}_i) = \left\| \hat{\mathcal{X}}_j^{\mathrm{m}}(\mathbf{x}_i) - \mathcal{X}_j^{\mathrm{m}}(\mathbf{x}_i) \right\|^2, \tag{10}$$

where $\pi: \mathbb{R}^3 \mapsto \mathbb{R}^2$ is the function projecting a node coordinate from the 3D calibration model space to the 2D camera/projector image space. Finally, Eq. 7 is minimized to obtain the camera and projector parameters and SL node 3D coordinates:

$$\left\{\hat{\theta}^{\mathrm{c}}, \hat{\theta}^{\mathrm{p}}, \hat{\mathcal{X}}^{\mathrm{m}}_{1:N_{\text{pose}}}\right\} = \underset{\theta^{\mathrm{c}}, \theta^{\mathrm{p}}, \mathcal{X}^{\mathrm{m}}_{1:N_{\text{pose}}}}{\arg\min}\ \text{loss}_{\text{BA}}\left(\theta^{\mathrm{c}}, \theta^{\mathrm{p}}, \mathcal{X}^{\mathrm{m}}_{1:N_{\text{pose}}}\right), \tag{11}$$

where $\hat{\mathcal{X}}_{1:N_{\text{pose}}}$ are optimized SL node coordinates, $\theta^{\mathrm{c}} = \left(\mathbf{K}^{\mathrm{c}}, \mathbf{d}^{\mathrm{c}}, \mathbf{r}^{\mathrm{mc}}_{1:N_{\text{pose}}}, \mathbf{t}^{\mathrm{mc}}_{1:N_{\text{pose}}}\right)$ and $\theta^{\mathrm{p}} = (\mathbf{K}^{\mathrm{p}}, \mathbf{d}^{\mathrm{p}}, \mathbf{R}^{\mathrm{cp}}, \mathbf{t}^{\mathrm{cp}})$ are camera and

Table 1: Comparison of calibration reprojection errors between Moreno & Taubin [36], Huang *et al*. [21] and Ours in different imaging settings.

Setting	RMSE^c↓			RMSE^p↓			RMSE^{stereo}↓		
	Moreno & Taubin	Huang	Ours	Moreno & Taubin	Huang	Ours	Moreno & Taubin	Huang	Ours
Setting1	**0.1542**	0.2403	0.2373	0.6966	0.2614	**0.2608**	0.5045	0.2511	**0.2493**
Setting2	**0.1397**	0.2165	0.2213	1.2378	0.2201	**0.2049**	0.8808	0.2183	**0.2132**
Setting3	**0.2251**	0.2428	0.2322	0.8638	0.2271	**0.2129**	0.6312	0.2351	**0.2228**
Setting4	**0.1712**	0.2619	0.2348	2.6071	0.1790	**0.1615**	1.8475	0.2243	**0.2015**
Setting5	0.4047	0.2487	**0.2309**	2.0323	0.1835	**0.1680**	1.4653	0.2185	**0.2019**
Setting6	0.4904	0.3387	**0.2378**	2.0266	0.5322	**0.2318**	1.4744	0.4461	**0.2348**
Setting7	**0.1290**	12.4804	0.2495	1.2099	13.5481	**0.2222**	0.8603	13.0252	**0.2363**

projector parameters, respectively. Denote $\mathcal{X}_j^{\mathrm{m}} = \bigcup_{i=1}^{M_j} \mathcal{X}_j^{\mathrm{m}}(\mathbf{x}_i)$ as the set of M_j SL node 3D coordinates at the j-th calibration board pose, then $\mathcal{X}_{1:N_{\mathrm{pose}}}^{\mathrm{m}} = \bigcup_{j=1}^{N_{\mathrm{pose}}} \mathcal{X}_j^{\mathrm{m}}$ is a union set of SL node 3D coordinates from all N_{pose} board poses.

After system calibration, we also apply the adaptive color SL pattern to single-shot-per-pose shape reconstruction. First, we project the color SL pattern to the target object, and capture it using the camera. Then, we find the projector-camera pixel correspondences by decoding the SL pattern, as shown in Fig. 4. Finally, we calculate the world coordinates of each pixel pair using the calibration parameter and a triangulation algorithm. For objects with complex geometry, we perform multiview shape reconstruction by applying our single-shot-per-pose reconstruction to different views. Then, we merge each view's point cloud using iterative closest point (ICP) [4], as shown in Fig. 9.

4 Experiments

We conduct a series of experiments to show the practicability and advantages of our adaptive color SL method. The experiment setups consist of different ambient light conditions, imaging devices' color responses, and calibration and shape reconstruction tasks are performed to evaluate compared methods.

Our projector-camera system setup consists of a Logitech c270i webcam and an EPSON CB-965 projector. In front of the projector-camera pair, a calibration board is positioned 0.7 to 3 meters away. An iPad Pro 2020 is employed to generate the ground truth point cloud of target objects, and a YN300Air II RGB fill light and room light are used to create different ambient light conditions.

4.1 Compared methods

The first compared method is Huang's method [21], which uses a fixed color SL pattern and Otsu's method [37] for color detection; while our method uses an adaptive color SL pattern and MAP-based color detection algorithm, termed Ours. Additionally, we also compare with a time multiplexing method Moreno & Taubin [36], a popular open source multi-shot Gray-coded SL for high quality projector-camera systems calibration and 3D reconstruction.

4.2 Experimental evaluations

We compare color detection and grid segmentation metrics such as color detection accuracy (**Accuracy**) (Fig. 4 step 4), number of extracted nodes (Fig. 4 step 3) and decoded nodes (Fig. 4 step 6). To evaluate the system calibration task, our criteria take into account the Root Mean Square Error (RMSE) for camera reprojection (RMSE^c), projector reprojection (RMSE^p), stereo reprojection (RMSE^{stereo}),

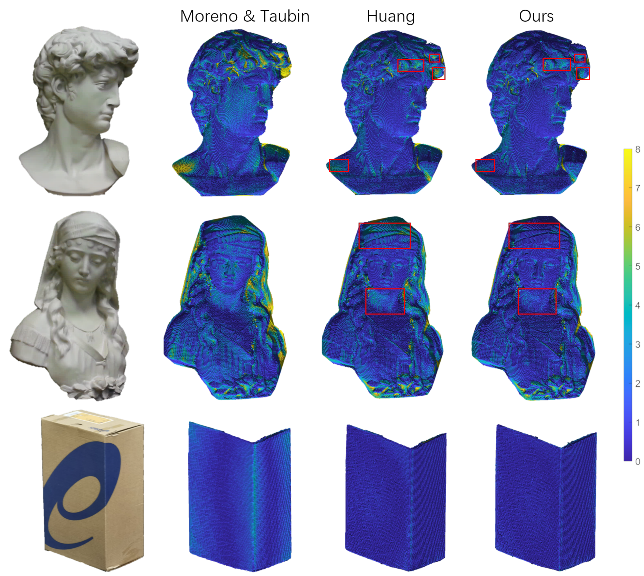

Figure 7: Qualitative comparisons of calibration. Camera-captured objects (1st column). Reconstructed David (1st row), girl (2nd row) and box (3rd row) using a projector-camera pair calibrated by the three calibration methods in Setting2. RMS point cloud alignment errors, i.e., RMSE^{align} (mm) are shown in pseudocolor. Moreno & Taubin's method [36] has the largest alignment error among the three methods.

and point cloud alignment (RMSE^{align}) errors as defined below:

$$\mathrm{RMSE}^{\mathrm{c}} = \mathrm{sqrt}\left(\frac{1}{n_p}\sum_{j=1}^{N_{\mathrm{pose}}}\sum_{i=1}^{M_j}\delta_j^{\mathrm{c}}(\mathbf{x}_i)\right) \tag{12}$$

$$\mathrm{RMSE}^{\mathrm{p}} = \mathrm{sqrt}\left(\frac{1}{n_p}\sum_{j=1}^{N_{\mathrm{pose}}}\sum_{i=1}^{M_j}\delta_j^{\mathrm{p}}(\mathbf{x}_i)\right) \tag{13}$$

$$\mathrm{RMSE}^{\mathrm{stereo}} = \mathrm{sqrt}\left(\frac{1}{2n_p}\sum_{j=1}^{N_{\mathrm{pose}}}\sum_{i=1}^{M_j}\left(\delta_j^{\mathrm{c}}(\mathbf{x}_i)+\delta_j^{\mathrm{p}}(\mathbf{x}_i)\right)\right) \tag{14}$$

$$\mathrm{RMSE}^{\mathrm{align}} = \mathrm{sqrt}\left(\frac{1}{n_p}\sum_{j=1}^{N_{\mathrm{pose}}}\sum_{i=1}^{M_j}\left\|\bar{\mathcal{X}}_j^{\mathrm{m}}(\mathbf{x}_i)-\hat{\mathcal{X}}_j^{\mathrm{m}}(\mathbf{x}_i)\right\|^2\right) \tag{15}$$

where $\bar{\mathcal{X}}_j^{\mathrm{m}}(\mathbf{x}_i)$ is the ground truth coordinate of a point $\mathbf{x}_i$ in the model space and $\hat{\mathcal{X}}_j^{\mathrm{m}}(\mathbf{x}_i)$ is the reconstructed coordinate in the model space using the calibrated parameters $\hat{\theta}^{\mathrm{c}}$, $\hat{\theta}^{\mathrm{p}}$. M_j is the number of SL node 3D coordinates at the j-th calibration board pose and the total number of points from N_{pose} poses is given by

Ambient light	Light1	Light2	Light3	Light4	Light5	Light6
Sample image	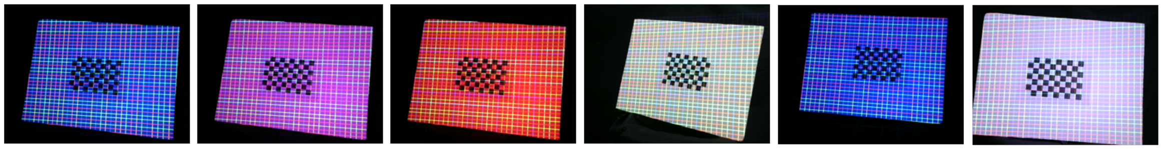					
RGB fill light	RGB=(0, 0, 40)	RGB=(50, 0, 50)	RGB=(99, 0, 0)	Off	RGB=(0, 0, 99)	RGB=(50, 50, 50)
Room light	Off	Off	Off	On	Off	On

Figure 8: Different ambient light conditions used for comparison. See supplementary for more poses.

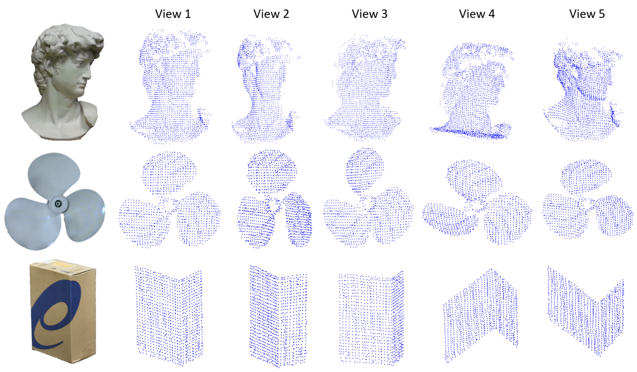

Figure 9: Merged point clouds generated by our adaptive color SL. The three rows are *David*, *fan* and *box*, respectively. The 1st column shows the RGB image and the rest columns are different views of the point clouds.

$n_p = \sum_{j=1}^{N_{\text{pose}}} M_j$.

4.2.1 Color response

In this experiment, we set the numbers of color labels for both horizontal and vertical stripes in Huang's [21] and our SL pattern to 4, i.e., $N_{\text{hori}} = N_{\text{vert}} = 4$. We only change the imaging settings of the projector and the camera, e.g., we use different projector and camera color responses and resolutions. As shown in Fig. 6, Setting1 is carefully adjusted such that the camera-captured colors look similar to the projector input ones. Setting2 to Setting6 are non-ideal settings, and the camera-captured colors are noticeably different from the projector input ones. Setting7 is an extreme setting where the camera-captured colors significantly deviate from the projector input ones. We also conduct experiments in other extreme image settings different from Setting7. It should be noted that the images in Fig. 6 and Fig. 8 are sample images with similar views. For each imaging setting, we captured at least 10 different calibration board poses, see supplementary material for more results.

Color detection and grid segmentation. We compare color detection and grid segmentation performance between Huang's fixed color SL pattern [21] and the proposed method, the results are shown in Tab. 3. Setting1 is an ideal imaging setting, which is intentionally used to show that without color distortions, the grid segmentation and color detection results of [21] and ours are similar. Setting2 to Setting7 are non-ideal settings, and Huang's [21] color detection and grid segmentation results are unsatisfactory. For example, in Setting4, the blue subgrid is not clear due to the high saturation and warm color temperature, causing poor blue subgrid segmentation. In contrast, our adaptive color SL method uses segmentation success rate to constrain the solution of optimal color combination, forcing the SL pattern's colors to be both distinct and easy to segment.

We also experiment with high-resolution settings in Setting5 and Setting6. As shown in Tab. 3, it is evident that our adaptive SL can extract and decode more color grid nodes, which are vital to the subsequent system calibration and shape reconstruction tasks. Overall, our adaptive color SL pattern and MAP-based color detection algorithm together bring constantly higher color detection accuracy and more color grid nodes in different imaging settings.

Calibration and reconstruction. Calibration comparisons are shown in Tab. 1, and it is clear that our method has lower projector and stereo reprojection RMSEs for different settings. Clearly, our method has lower projector and stereo reprojection RMSEs than Moreno & Taubin [36] and Huang *et al*. [21]. In particular, for Setting7 Huang has high reprojection RMSEs due to high proportion of incorrectly decoded color grid nodes, while our method can still work. Because of the adaptive color SL pattern and MAP-based color detection algorithm, our method not only has a smaller calibration error in different settings but can also work in an extreme imaging setting.

It is worth noting that Moreno & Taubin's [36] projector and stereo reprojection RMSEs are larger than the proposed method, because the projector and stereo reprojection RMSEs are calculated using a different formula from Moreno & Taubin [36]'s software, since we also include the extrinsic parameters $\mathbf{r}^{\text{cp}}$ and $\mathbf{t}^{\text{cp}}$ in the projector and stereo RMSEs equations to better evaluate extrinsics calibration accuracy (see Eq. 9, Eq. 13 and Eq. 14). Moreover, Moreno & Taubin [36] do not use BA to deal with imperfect planarity of the calibration board.

The obtained calibration parameters, i.e., θ^{c}, θ^{p} of the three methods are also used to reconstruct point clouds for different real objects using Moreno & Taubin's [36] Gray-coded SL patterns. An iPad Pro 2020 trueDepth camera is used to obtain ground truth point clouds [45]. Point cloud alignment errors ($\text{RMSE}^{\text{align}}$) are calculated and compared among the three methods. However, it should be noted that point clouds generated by iPad Pro 2020 have a different coordinate system. To calculate the alignment error, we use ICP [4] to align the point cloud to the ground truth before calculating point cloud alignment errors. The alignment errors of different real objects, i.e., David (mm), girl (mm) and box (mm), are shown in supplementary. Qualitative comparisons are shown in Fig. 7. Clearly, our method has the lowest mean point cloud alignment errors, due to our higher calibration accuracy.

We also apply our adaptive color SL to the shape reconstruction task. We set the number of color labels of the horizontal stripes to 4, and the number of vertical stripes to 5 for our adaptive color SL in this experiment. The experimental results are compared with Huang's fixed color SL [21], and their reconstruction results are both based on the same calibrated geometric parameters.

We conduct the experiment in a carefully tuned setting, where the camera resolution is 1280×960, the projector resolution is 1920×1080, and the other parameters are similar to Setting1 of Fig. 6. We also apply both methods to scan the object from different views (about 7-12 shots) and merge the point clouds using

Table 2: Comparison of calibration reprojection errors of Moreno & Taubin [36], Huang *et al*. [21] and Ours under different ambient light conditions.

Light	$\text{RMSE}^{c}\downarrow$			$\text{RMSE}^{p}\downarrow$			$\text{RMSE}^{stereo}\downarrow$		
	Moreno & Taubin	Huang	Ours	Moreno & Taubin	Huang	Ours	Moreno & Taubin	Huang	Ours
Light1	**0.1639**	0.2381	0.2349	2.0851	0.1880	**0.1844**	1.4790	0.2145	**0.2111**
Light2	**0.1545**	0.2352	0.2353	1.9476	0.1884	**0.1883**	1.3815	**0.2131**	0.2131
Light3	**0.1764**	0.2573	0.2417	1.9410	0.2223	**0.1886**	1.3781	0.2405	**0.2168**
Light4	**0.1732**	0.2291	0.2243	2.1967	0.1920	**0.1775**	1.5582	0.2114	**0.2023**
Light5	**0.2181**	1.7906	0.2371	1.0249	83.9224	**0.1994**	0.7409	59.3556	**0.2191**
Light6	**0.1554**	6.5740	0.2176	3.6754	7.6561	**0.1761**	2.6012	7.1356	**0.1979**

Table 3: Comparison of color detection accuracy, #extracted nodes and decoded nodes between Huang's [21] and our method in different imaging settings. Setting1 is an ideal setting.

Setting	Accuracy↑		#Extr. nodes↑		#Deco. nodes↑	
	Huang	Ours	Huang	Ours	Huang	Ours
Setting1	0.9438	**0.9630**	**3388**	3381	**2255**	1992
Setting2	0.8837	**0.9522**	**3109**	3102	1428	**1889**
Setting3	0.8774	**0.9546**	**3578**	3456	1470	**2108**
Setting4	0.8353	**0.9503**	3814	**5010**	1064	**2609**
Setting5	**0.9265**	0.9209	6788	**8782**	3099	**4424**
Setting6	**0.9054**	0.8563	9938	**10254**	4477	**5147**
Setting7	0.7179	**0.8882**	3916	**4118**	771	**2043**

Table 4: Comparison of color detection accuracy, #extracted nodes and decoded nodes between Huang's [21] and our method under different ambient light conditions.

Light	Accuracy↑		#Extr. nodes↑		#Deco. nodes↑	
	Huang	Ours	Huang	Ours	Huang	Ours
Light1	0.7739	**0.9230**	5498	**5512**	1938	**3170**
Light2	0.7905	**0.8863**	5487	**5505**	1701	**2950**
Light3	0.7938	**0.8462**	5563	**5571**	1993	**2923**
Light4	0.7842	**0.8976**	**5699**	5674	1327	**3034**
Light5	0.7198	**0.8857**	**7021**	6993	1077	**3596**
Light6	0.7752	**0.8408**	8290	**8888**	2526	**4549**

ICP [4]. As shown in Fig. 9, because Huang's fixed pattern [21] has few points, the point cloud merge failed and is excluded from the figure. The number of reconstructed points and RMS point cloud alignment errors are shown in supplementary. Shape reconstruction experiments in an extreme setting are also shown in supplementary.

4.2.2 Ambient light

To further evaluate the robustness of our adaptive color SL under different ambient light conditions. We keep the camera resolution at 640×480 and the projector resolution at 1024×768, and also keep their color responses as ideal. The numbers of color labels for both horizontal and vertical stripes in Huang's [21] and our SL pattern are set to 4, i.e., $N_{\text{hori}} = N_{\text{vert}} = 4$. We only change the RGB fill light and room light to create different ambient light conditions, as shown in Fig. 8. It should be noted that room light is used to introduce strong ambient light, such that the camera-captured image maybe overexposed, as shown in Fig. 8 Light4 and Light6, the images are severely washed out due to the strong room light.

Color detection and grid segmentation. The color detection and grid segmentation performance under different ambient light conditions are shown in Tab. 4. It can be noticed that under different ambient light conditions, Huang's [21] color detection accuracy is lower than our method, due to three reasons: (1) The colors of Huang's color grid are heavily polluted by ambient light, as shown in Fig. 8 Light1, Light2, Light3 and Light5. (2) As shown in Fig. 8, the ambient light produced by the RGB fill light and room light causes nonuniform light intensities on the calibration board, leading to inconsistent hue distributions on the board surface and also in different board positions. While Huang *et al*. [21] use Otsu's [37] for color detection, which assumes consistent hue distributions across the entire board surface and all poses. Thus, Huang's method performs much worse under different ambient light conditions (Tab. 4) than under different imaging settings (Tab. 3). (3) Huang's method [21] is sensitive to overexposed ambient light conditions as shown in Fig. 8 Light4 and Light6, while our method effectively excludes colors that are easily affected by ambient light during adaptive color SL pattern generation. In addition, our MAP-based color detection algorithm adds robustness to nonuniform and slightly overexposed ambient light conditions.

Overall, Huang's fixed color SL [21] is more sensitive to ambient light, while our method constantly outperforms it on color detection accuracy, the number of extracted and decoded nodes, due to the adaptive color SL pattern and MAP-based color detection.

Calibration and reconstruction. We also compare our method with Huang's fixed color SL [21] on calibration tasks, under different ambient light conditions. Observing the calibration results in Tab. 2, we find that the proposed method has constantly lower projector and stereo reprojection errors, which demonstrates that our method can also adapt to different ambient light conditions. Same as § 4.2.1, the calibration parameters, i.e., θ^{c}, θ^{p} obtained by the three methods are used for shape reconstruction comparison. The mean alignment errors of shape reconstruction for different real objects are shown in supplementary and our method is more robust against different ambient light conditions. Ablation studies on the effectiveness of adaptive color SL and MAP-based color detection are given in supplementary.

5 Conclusion and Limitations

In this paper, we propose an adaptive color SL that can adapt to different ambient light conditions and imaging device color responses. Our novel efficient color adaptation and MAP-based color detection methods show clear advantages in experiments compared with fixed color SL. Moreover, our method does not require a preliminary response function calibration or geometric calibration step, making it more practical for arbitrary setups. Our method also has some limitations, e.g., our method needs to regenerate the adaptive color SL when the imaging settings or ambient light conditions change. (2) The projector-camera intrinsics and extrinsics need recalibration when the relative projector-camera poses or focal length change.

Acknowledgments

This work was supported in part by Fundamental Research Funds for the Central Universities (SWU-KQ22004). Ling was not supported by any research fund for this work.

References

[1] H. Anwar, I. Din, and K. Park. Projector calibration for 3d scanning using virtual target images. *International Journal of Precision Engineering and Manufacturing*, 13(1):125–131, 2012.

[2] A. Ben-Hamadou, C. Soussen, C. Daul, W. Blondel, and D. Wolf. Flexible calibration of structured-light systems projecting point patterns. *Computer Vision and Image Understanding*, 117(10):1468–1481, 2013.

[3] F. Berryman, P. Pynsent, J. Fairbank, and S. Disney. A new system for measuring three-dimensional back shape in scoliosis. *European Spine Journal*, 17(5):663–672, 2008.

[4] P. J. Besl and N. D. McKay. Method for registration of 3-d shapes. In *Sensor Fusion IV: Control Paradigms and Data Structures*, vol. 1611, pp. 586–606. SPIE, 1992.

[5] K. L. Boyer and A. C. Kak. Color-encoded structured light for rapid active ranging. *IEEE Transactions on Pattern Analysis and Machine Intelligence*, 9(1):14–28, 1987.

[6] D. Caspi, N. Kiryati, and J. Shamir. Range imaging with adaptive color structured light. *IEEE Transactions on Pattern Analysis and Machine Intelligence*, 20(5):470–480, 1998.

[7] L. Chen, X. Wang, and S. Chen. Shape acquisition using a color stripe pattern with stereo structure. In *Proceedings of the World Congress on Intelligent Control and Automation*, pp. 1014–1017. IEEE, 2014.

[8] N. de Bruijn. A combinatorial problem. *Proceedings of the Section of Sciences of the Koninklijke Nederlandse Akademie van Wetenschappen te Amsterdam*, 49(7):758–764, 2022.

[9] P. Fechteler and P. Eisert. Adaptive colour classification for structured light systems. *IET Computer Vision*, 3(2):49–59, 2009.

[10] P. Fechteler, P. Eisert, and J. Rurainsky. Fast and high resolution 3d face scanning. In *IEEE International Conference on Image Processing*, vol. 3, pp. III–81–III–84. IEEE, 2007.

[11] Y. Fujimoto, T. Sawabe, M. Kanbara, and H. Kato. Structured light of flickering patterns having different frequencies for a projector-event-camera system. In *IEEE Conference on Virtual Reality and 3D User Interfaces*, pp. 582–588. IEEE, 2022.

[12] K. Fukamizu, L. Miyashita, and M. Ishikawa. Elamorph projection: Deformation of 3d shape by dynamic projection mapping. In *IEEE International Symposium on Mixed and Augmented Reality*, pp. 164–173. IEEE, 2020.

[13] N. Gard, A. Hilsmann, and P. Eisert. Projection distortion-based object tracking in shader lamp scenarios. *IEEE Transactions on Visualization and Computer Graphics*, 25(11):3105–3113, 2019.

[14] J. Geng. Structured-light 3d surface imaging: a tutorial. *Advances in Optics and Photonics*, 3(2):128–160, 2011.

[15] A. Grundhöfer and D. Iwai. Robust, error-tolerant photometric projector compensation. *IEEE Transactions on Image Processing*, 24(12):5086–5099, 2015.

[16] F. Heinrich, L. Schwenderling, F. Joeres, K. Lawonn, and C. Hansen. Comparison of augmented reality display techniques to support medical needle insertion. *IEEE Transactions on Visualization and Computer Graphics*, 26(12):3568–3575, 2020.

[17] Z. Hu, Q. Guan, S. Liu, and S. Chen. Robust 3d shape reconstruction from a single image based on color structured light. In *International Conference on Artificial Intelligence and Computational Intelligence*, vol. 3, pp. 168–172. IEEE, 2009.

[18] B. Huang and H. Ling. DeProCams: Simultaneous relighting, compensation and shape reconstruction for projector-camera systems. *IEEE Transactions on Visualization and Computer Graphics*, 27(5):2725–2735, 2021.

[19] B. Huang, T. Sun, and H. Ling. End-to-end full projector compensation. *IEEE Transactions on Pattern Analysis and Machine Intelligence*, 44(6):2953–2967, 2021.

[20] B. Huang and Y. Tang. Fast 3d reconstruction using one-shot spatial structured light. In *IEEE International Conference on Systems, Man, and Cybernetics*, pp. 531–536. IEEE, 2014.

[21] B. Huang, Y. Tang, S. Ozdemir, and H. Ling. A fast and flexible projector-camera calibration system. *IEEE Transactions on Automation Science and Engineering*, 18(3):1049–1063, 2020.

[22] L. Huang, P. S. K. Chua, and A. Asundi. Least-squares calibration method for fringe projection profilometry considering camera lens distortion. *Applied Optics*, 49(9):1539–1548, 2010.

[23] C. Je, S. W. Lee, and R.-H. Park. Colour-stripe permutation pattern for rapid structured-light range imaging. *Optics Communications*, 285(9):2320–2331, 2012.

[24] J. N. Jensen, M. Hannemose, J. A. Bærentzen, J. Wilm, J. R. Frisvad, and A. B. Dahl. Surface reconstruction from structured light images using differentiable rendering. *Sensors*, 21(4):1068, 2021.

[25] S. Kagami and K. Hashimoto. Animated stickies: Fast video projection mapping onto a markerless plane through a direct closed-loop alignment. *IEEE Transactions on Visualization and Computer Graphics*, 25(11):3094–3104, 2019.

[26] H. Kawasaki, R. Furukawa, R. Sagawa, and Y. Yagi. Dynamic scene shape reconstruction using a single structured light pattern. In *IEEE Conference on Computer Vision and Pattern Recognition*, pp. 1–8. IEEE, 2008.

[27] V. Klein, M. Leuschner, T. Langen, P. Kurth, M. Stamminger, and F. Bauer. Scan&paint: Image-based projection painting. In *IEEE International Symposium on Mixed and Augmented Reality*, pp. 517–525. IEEE, 2021.

[28] T. Koninckx and L. Van Gool. Real-time range acquisition by adaptive structured light. *IEEE Transactions on Pattern Analysis and Machine Intelligence*, 28(3):432–445, 2006.

[29] T. P. Koninckx, P. Peers, P. Dutré, and L. Van Gool. Scene-adapted structured light. In *IEEE Conference on Computer Vision and Pattern Recognition*, vol. 2, pp. 611–618. IEEE, 2005.

[30] P. Kurth, V. Lange, C. Siegl, M. Stamminger, and F. Bauer. Auto-calibration for dynamic multi-projection mapping on arbitrary surfaces. *IEEE Transactions on Visualization and Computer Graphics*, 24(11):2886–2894, 2018.

[31] P. Kurth, V. Lange, M. Stamminger, and F. Bauer. Real-time adaptive color correction in dynamic projection mapping. In *IEEE International Symposium on Mixed and Augmented Reality*, pp. 174–184. IEEE, 2020.

[32] K. H. Lee, C. Je, and S. W. Lee. Color-stripe structured light robust to surface color and discontinuity. In *Asian Conference on Computer Vision*, pp. 507–516. Springer, 2007.

[33] M. Maruyama and S. Abe. Range sensing by projecting multiple slits with random cuts. *IEEE Transactions on Pattern Analysis and Machine Intelligence*, 15(6):647–651, 1993.

[34] Y. Mikawa, C. Eichhorn, and G. Klinker. Multi-color led marker for dynamic target tracking in wide area. In *IEEE Conference on Virtual Reality and 3D User Interfaces Abstracts and Workshops*, pp. 669–670, 2023. doi: 10.1109/VRW58643.2023.00177

[35] Y. Mikawa, T. Sueishi, Y. Watanabe, and M. Ishikawa. Dynamic projection mapping for robust sphere posture tracking using uniform/biased circumferential markers. *IEEE Transactions on Visualization and Computer Graphics*, 28(12):4016–4031, 2021.

[36] D. Moreno and G. Taubin. Simple, accurate, and robust projector-camera calibration. In *International Conference on 3d Imaging, Modeling, Processing, Visualization & Transmission*, pp. 464–471. IEEE, 2012.

[37] N. Otsu. A threshold selection method from gray-level histograms. *IEEE Transactions on Systems, Man, and Cybernetics*, 9(1):62–66, 1979.

[38] E. Peillard, Y. Itoh, G. Moreau, J.-M. Normand, A. Lécuyer, and F. Argelaguet. Can retinal projection displays improve spatial perception in augmented reality? In *IEEE International Symposium on Mixed and Augmented Reality*, pp. 80–89. IEEE, 2020.

[39] T. Petković, T. Pribanić, and M. Đonlić. Single-shot dense 3d reconstruction using self-equalizing de bruijn sequence. *IEEE Transactions on Image Processing*, 25(11):5131–5144, 2016.

[40] P. Pjanic, S. Willi, D. Iwai, and A. Grundhöfer. Seamless multi-projection revisited. *IEEE Transactions on Visualization and Computer Graphics*, 24(11):2963–2973, 2018.

[41] R. Sagawa, Y. Ota, Y. Yagi, R. Furukawa, N. Asada, and H. Kawasaki. Dense 3d reconstruction method using a single pattern for fast moving object. In *International Conference on Computer Vision*, pp. 1779–1786. IEEE, 2009.

[42] J. Salvi, S. Fernandez, T. Pribanic, and X. Llado. A state of the art in structured light patterns for surface profilometry. *Pattern Recognition*,

43(8):2666–2680, 2010.

[43] M. A. Tehrani, A. Saghaeian, and O. R. Mohajerani. A new approach to 3d modeling using structured light pattern. In *International Conference on Information and Communication Technologies: From Theory to Applications*, pp. 1–5. IEEE, 2008.

[44] T. van Aardenne-Ehrenfest and N. G. de Bruijn. Circuits and trees in oriented linear graphs. *Classic papers in combinatorics*, pp. 149–163, 1987.

[45] M. Vogt, A. Rips, and C. Emmelmann. Comparison of ipad pro®'s lidar and truedepth capabilities with an industrial 3d scanning solution. *Technologies*, 9(2):25, 2021.

[46] S. Willi and A. Grundhöfer. Robust geometric self-calibration of generic multi-projector camera systems. In *IEEE International Symposium on Mixed and Augmented Reality*, pp. 42–51. IEEE, 2017.

[47] M. Yue, J. Wang, J. Zhang, Y. Zhang, Y. Tang, and X. Feng. Color crosstalk correction for synchronous measurement of full-field temperature and deformation. *Optics and Lasers in Engineering*, 150:106878, 2022. doi: 10.1016/j.optlaseng.2021.106878

[48] B. Zhang, Y. Li, and Y. Wu. Self-recalibration of a structured light system via plane-based homography. *Pattern Recognition*, 40(4):1368–1377, 2007.

[49] L. Zhang, B. Curless, and S. M. Seitz. Rapid shape acquisition using color structured light and multi-pass dynamic programming. In *International Symposium on 3d Data Processing Visualization and Transmission*, pp. 24–36. IEEE, 2002.

[50] S. Zhang and P. S. Huang. Novel method for structured light system calibration. *Optical Engineering*, 45(8):083601, 2006.

[51] X. Zhang, Y. Li, and L. Zhu. Color code identification in coded structured light. *Applied Optics*, 51(22):5340–5356, 2012.

[52] Z. Zhang. A flexible new technique for camera calibration. *IEEE Transactions on Pattern Analysis and Machine Intelligence*, 22(11):1330–1334, 2000.

[53] Y. Zhou, D. Zhao, Y. Yu, J. Yuan, and S. Du. Adaptive color calibration based one-shot structured light system. *Sensors*, 12(8):10947–10963, 2012.

[54] M. Đonlić, T. Petković, and T. Pribanić. 3d surface profilometry using phase shifting of De Bruijn pattern. In *International Conference on Computer Vision*, 2015.